


Communication

Facile Preparation of Au–Ag Composite Nanostructure for High-Sensitive and Uniform Surface-Enhanced Raman Spectroscopy

Wenjie Liu ¹, Zhonghua Yan ¹, Weina Zhang ¹, Kunhua Wen ², Bo Sun ¹, Xiaolong Hu ^{3,*} and Yuwen Qin ¹ 

- ¹ Guangdong Provincial Key Laboratory of Photonics Information Technology, School of Information Engineering, Guangdong University of Technology, Guangzhou 510006, China
² School of Physics and Optoelectronic Engineering, Guangdong University of Technology, Guangzhou 510006, China
³ Engineering Research Center for Optoelectronics of Guangdong Province, School of Physics and Optoelectronics, South China University of Technology, Guangzhou 510640, China
 * Correspondence: scxihu@scut.edu.cn

Abstract: Preparation of a high-sensitive and uniform surface-enhanced Raman spectroscopy (*SERS*) active substrate structure usually faces complex processes and high costs. Here, porous Au–Ag composite nanostructures that are conventionally fabricated by the deposition of a multilayer Au–Ag, annealing, and dealloying process are proposed for high-performance *SERS*. By annealing at a suitable temperature, nanopores could be firmly distributed on the surface, which serves as hot spots. The electric field distribution was also performed by the finite difference time domain. The experiment results exhibited excellent uniformity and high sensitivity of *SERS* detection. The enhancement factor of the R6G molecules detected by the *SERS* substrate reached 1.37×10^7 , and the relative standard deviation was as low as 4.9%. The minimum detection concentration of R6G molecules by the Au–Ag composite nanostructures with bottom Au mirror could reach 10^{-13} M. The proposed Au–Ag composite nanostructures and the fabrication process have great potential in preparation of a high-sensitive and uniform *SERS* substrate.

Keywords: *SERS*; porous Au–Ag; high-sensitivity; uniform; annealing



Citation: Liu, W.; Yan, Z.; Zhang, W.; Wen, K.; Sun, B.; Hu, X.; Qin, Y. Facile Preparation of Au–Ag Composite Nanostructure for High-Sensitive and Uniform Surface-Enhanced Raman Spectroscopy. *Photonics* **2023**, *10*, 354. <https://doi.org/10.3390/photonics10040354>

Received: 3 March 2023
 Revised: 17 March 2023
 Accepted: 20 March 2023
 Published: 23 March 2023



Copyright: © 2023 by the authors. Licensee MDPI, Basel, Switzerland. This article is an open access article distributed under the terms and conditions of the Creative Commons Attribution (CC BY) license (<https://creativecommons.org/licenses/by/4.0/>).

1. Introduction

Surface-enhanced Raman scattering (*SERS*) is a nondestructive and ultra-sensitive spectroscopic technique that has been widely used in biomedicine [1–4], food safety [5–9], environmental monitoring [10,11], etc. An ideal *SERS* substrate requires excellent signal enhancement, hot spot uniformity, high stability, and facile fabrication [12,13]. *SERS* enhancement is mainly attributed to electromagnetic (EM) enhancement proportional to the fourth power of the local electric field intensity [14]. Localized surface plasmon resonance (LSPR) generated by metal nanostructures [15–17] or deep gaps [18–20] demonstrates an extremely strong electric field [21,22], which is widely used in Raman signal enhancement. Nanoparticles, such as nanospheres [23,24], nanotriangles [25], nanorods [26], and nanostars [27,28], could be prepared by chemical methods. However, the hot spots induced by the chemically prepared nanoparticles are randomly distributed due to the random aggregation, resulting in poor uniformity. In contrast, a uniform distribution of hot spots could be obtained through a physical method with ordered and periodic nanostructures [29,30], such as nano-peak arrays, double nano-ring arrays, nano-gratings, and ordered or periodic nanostructures formed by self-assembly. However, preparation of these nanostructures usually requires high manufacturing accuracy equipment, such as electron beam lithography, focused ion beam lithography, and nanoimprint lithography, thus significantly increasing manufacturing costs [31,32]. Furthermore, these methods are always accompanied by

limited fabrication areas or long fabrication times. Therefore, it is important to find a facile and large-area preparation method.

The surface structure and the material of the *SERS* substrate are two key factors affecting Raman signal intensity. For the surface structure, noble metal nanohole structures have attracted extensive attention due to their high density and embedded hotspots. For instance, Koya et al. showed that EM hotspots formed by metal nanoporous materials are widely used in surface-enhanced Raman spectroscopy [33]. Liu et al. fabricated porous gold nanoparticle structures through an ultra-thin alumina membrane incorporated with annealing and dealloying techniques, which showed marvelous uniformity and sensitivity in *SERS* analysis, and the Raman enhancement factor (*EF*) reached 1.4×10^7 with a relative standard deviation (RSD) less than 6.6% [34]. RSD represents the ratio of standard deviation to average. For the material of the *SERS* substrate, compared with Au nanoparticles, Ag nanoparticles have stronger local field enhancement factors in the visible light range; however, they have a relatively poor stability. The use of Au–Ag alloy materials can combine the strong plasmonic enhancement of Ag with the material stability of Au. Mandal et al. studied *SERS* results, showing that the intensity of the *SERS* substrate with Au–Ag bimetallic nanoparticles is stronger than that with monometallic nanoparticles [35]. Gao et al. reported that the *SERS* substrate with Au–Ag core-shell nanospheres exhibited strong coupling at a wavelength of 633 nm by a combination of the plasmonic properties induced by the Ag and the chemical stability induced by the Au [36]. However, the preparation process of Au–Ag alloy nanostructures is normally complex and requires nano-processing technology [37–39].

In this paper, a facile method is presented that depends on conventional metal deposition annealing and dealloying. Au–Ag nanostructures are formed by alternating the deposition of multilayer gold and silver, annealing at a low temperature, and the dealloying of the as-grown Au–Ag multilayer. By controlling the annealing temperature, the *EF* of the *SERS* substrate reached 2.4×10^5 . In addition, by adding a gold bottom mirror layer, the sensitivity and electric field strength was further improved, the *EF* was as high as 1.37×10^7 , and the RSD reached 4.9%.

2. Method

2.1. Sample Fabrication

The fabrication process of the composite Au–Ag alloy structure is shown in Figure 1. For sample 1, the preparation process was as follow: a 0.5 nm-thick Ti was first evaporated onto the Si substrate at a rate of 0.5 Å s^{-1} . Then, four layers of 10 nm Au and 20 nm Ag were alternately deposited; the surface Au–Ag alloy was formed by annealing for 30 s under nitrogen flow. The annealed porous Au–Ag alloy structure was immersed in the H_3PO_4 etching solution for 1 min to remove the Ag at room temperature, and then immediately washed by DI water. Finally, a large-scale surface porous Au–Ag alloy substrate was successfully finished.

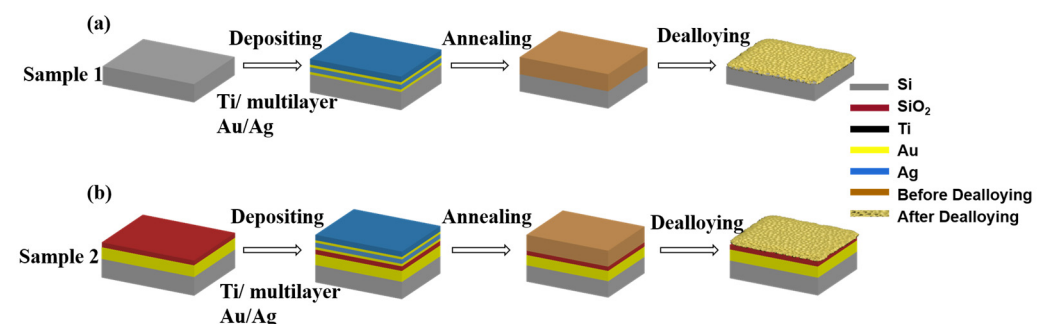


Figure 1. Schematic of the fabrication processes for (a) the porous Au–Ag structure and (b) the porous Au–Ag structure with bottom Au mirror by depositing, annealing, and dealloying techniques.

Here, the Au–Ag multilayer was adopted to fuse the metals more fully after annealing, resulting in denser and uniform holes after dealloying Ag. The preparation process of sample 2 is shown in the Figure 1b. Compared with sample 1, an additional bottom Au layer and an SiO₂ separation layer were added beneath the porous Au–Ag alloy. Then, the 60 nm bottom Au, 30 nm SiO₂, and 0.5 nm Ti layers were deposited. Finally, a porous Au–Ag alloy substrate with bottom Au was successfully prepared after the annealing and dealloying of the top Au–Ag multilayer.

2.2. Structural Characterization and SERS Measurements

The surface morphology of the samples was observed by a field emission scanning electron microscope (SEM), and the proportion of Au and Ag components on the surface of the samples was analyzed by an X-ray energy spectrometer. A rhodamine 6G (R6G) molecule was introduced as a probe molecule to characterize the SERS substrate performance of the Au–Ag composite nanostructures. The R6G aqueous solutions with different concentrations (10^{-6} – 10^{-13} M) were prepared. The samples were immersed in the prepared aqueous solution for 2 h and then dried by nitrogen flow. The Raman signals of the two samples were characterized by a 532 nm laser confocal Raman microscope with a laser power of 10 mW. The signal acquisition time was 9 s for R6G and the acquisition process was cycled three times to remove the spike noise.

2.3. Simulations

Three-dimensional finite-difference-time-domain (FDTD) was used to simulate the near-field EM field distribution. All boundaries were equipped with a perfectly matched layer (PML) condition. A plane wave with a wavelength of 532 nm as used to illuminate from the top, and the incident wave propagated perpendicular to the direction of the base surface. Field strength monitors were placed on the horizontal and vertical sections of the substrate to obtain the field strength distribution. The dielectric constants (ϵ) of Au–Ag alloys are represented by $\epsilon(\alpha) = \alpha\epsilon_{\text{Au}} + (1 - \alpha)\epsilon_{\text{Ag}}$, where $\alpha = 0.385$ (corresponding to the Au content in the Au–Ag alloys), and the dielectric constants of Au and Ag are taken from the data of Palik [40].

3. Results and Discussion

Figure 2a–e shows the SEM images of the Au–Ag composite nanostructures in sample 2 after annealing and dealloying processes. Sample 1 and sample 2 have a similar surface morphology at the same annealing temperature. From the intuitive view of the SEM images, Figure 2b shows that there is a thin layer of nano-network structure on the surface and Figure 2c shows a pore structure. The surface morphology of substrates under 200 °C and 300 °C was much more uniform than that of substrates at other temperatures. At the low annealing temperature, the porous structure could not be formed on the surface of the dealloyed structure and the Au and Ag were immersed in the etching solution. When the annealing temperature was greater than 400 °C, the Au–Ag structure after dealloying treatment formed a large area, and Ag in the alloy was difficult to be corroded by the etching solution to form a porous structure. Figure 2f shows the qualitative and quantitative analysis of the surface composition of the sample after annealing and dealloying by an X-ray energy dispersive spectrometer. It can be seen that as the annealing temperature increased, the proportion of Ag in the alloy increased, again confirming that the higher the annealing temperature, the more difficult it is to corrode the Ag in the alloy. A layer of Ti was needed as the adhesion layer between the Au–Ag structure and the Si substrate; otherwise, the structure may be unstable in the dealloying stage.

The SERS performance of the Au–Ag composite structure at different annealing temperatures is shown in Figure 3a. It was found that the SERS intensity first increased and then decreased with the increase in the annealing temperature. The intensity was sharply decreased with an annealing temperature greater than 300 °C. In addition, we digitally marked important bands in the Raman spectra. As shown in Figure 3b, the Raman intensity

peaks at the 603, 765, and 1178 cm^{-1} are plotted as a function of the annealing temperature. The Raman intensities of these peaks had a consistent increasing trend and the best *SERS* signal was obtained when the temperature was at 300 $^{\circ}\text{C}$.

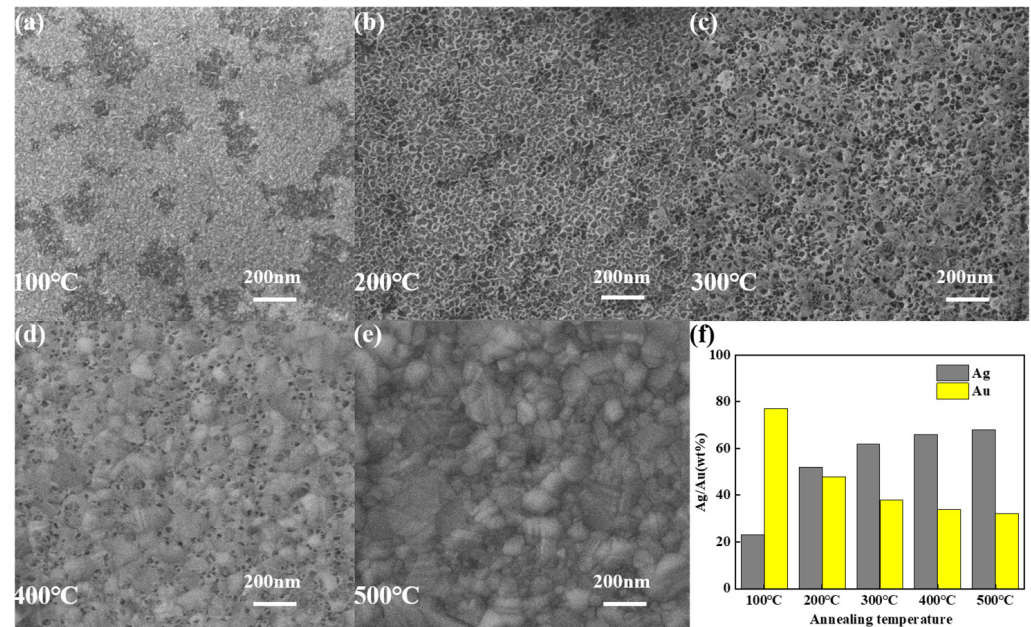


Figure 2. The SEM images of the Au-Ag composite nanostructures with different temperature of (a) 100 $^{\circ}\text{C}$, (b) 200 $^{\circ}\text{C}$, (c) 300 $^{\circ}\text{C}$, (d) 400 $^{\circ}\text{C}$, (e) 500 $^{\circ}\text{C}$, (f) The Au-Ag weight ratio as a function of annealing temperature.

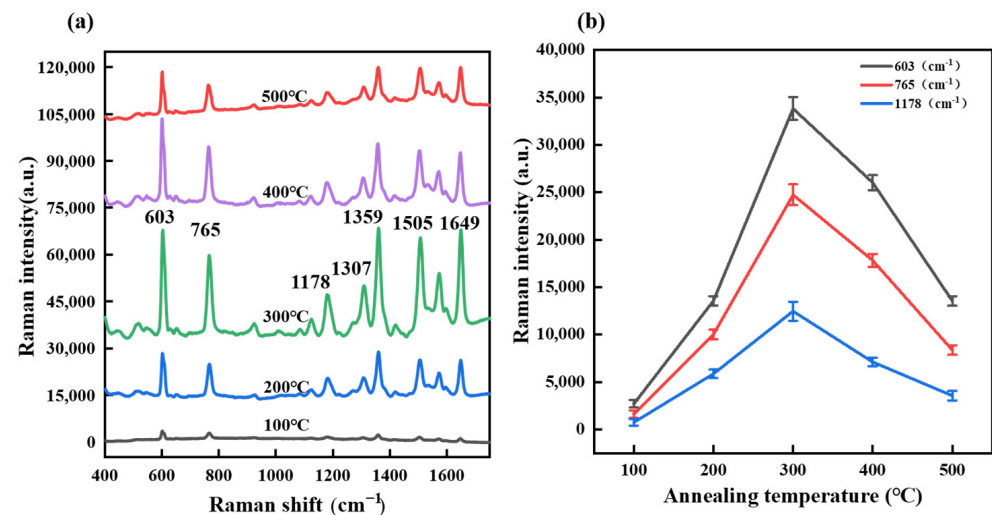


Figure 3. (a) The Raman spectra of the Au-Ag composite nanostructures with a series of annealing temperature from 100 $^{\circ}\text{C}$ to 500 $^{\circ}\text{C}$. (b) The Raman intensities at 603 cm^{-1} (black line), 765 cm^{-1} (red line), and 1178 cm^{-1} (blue line) peaks as a function of the annealing temperature.

Here, the FDTD simulation method was also used to analyze the distribution and intensity of the enhanced EM field on the surface of the *SERS* substrate. Figure 4a shows a simulation of the substrate without annealing and etching and Figure 4b,c shows an electric field ($\text{Re}(|E|)$) distribution cross-section (X-Y plane) of the composite nanostructures and the composite nanostructures with a bottom Au reflector, respectively. Compared with Figure 4b,c, it is obvious that the Au-Ag alloy nanostructures of sample 1 and sample 2 show a huge local field enhancement effect. The local field enhancement shown in Figure 4c was stronger than that shown in Figure 4b, which was due to the bottom Au layer reflecting

the light passing through the porous surface, enhancing the absorption [41]. Thus, the local field enhancement of the porous surface and the collection efficiency of *SERS* were improved. From the FDTD simulation, we demonstrated that the electric field intensity of Au–Ag nanostructures with gold mirrors was, on average, about 3.3 times that of the Au–Ag nanostructures without the bottom mirror.

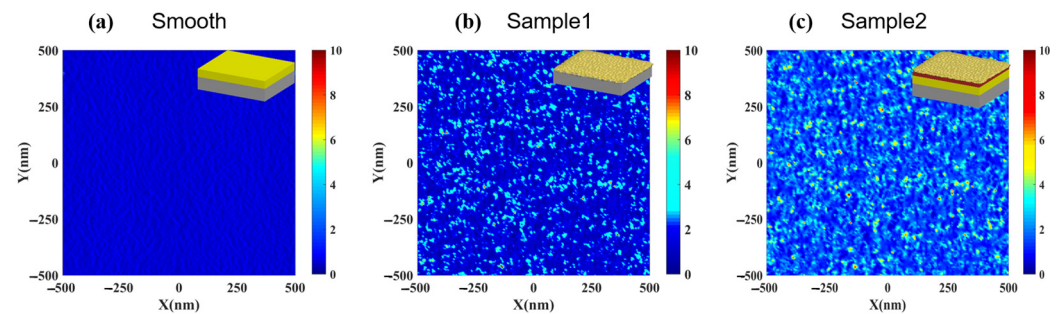


Figure 4. The simulated electric-field ($|E|$) distributions of the Au–Ag smooth structure without annealing (a) and Au–Ag composite nanostructures (b) and Au–Ag composite nanostructures with bottom Au mirror (c) under annealing temperature of 300 °C. The wavelength of plane wave irradiation is 532 nm and the insets are the side view of the numerical model corresponding to the electric field diagram.

In order to verify the effect of the Au–Ag composite nanostructure on the Raman signal enhancement, the substrates were immersed in R6G aqueous solutions of different concentrations and dried with nitrogen after 7 h. The Raman signal of the samples was characterized by a confocal Raman microscope with a 532 nm laser, and the integration time was 5 s. It can be seen from Figure 5a,b that the Raman signal intensity decreased with the dilution of the concentration; Raman signals can also be observed for both samples as the concentration was as low as 10^{-11} M. This indicates that the composite Au–Ag structure is very sensitive to R6G molecules. The minimum detectable concentration of the composite Au–Ag nanostructures with the bottom Au mirror can reach 10^{-13} M; three characteristic Raman peaks of R6G at 603, 765, and 1178cm^{-1} were selected to build the calibration curves of the Raman intensities as a function of R6G concentrations. The results show that the Raman intensity of the three characteristic peaks has a good linear correlation with the logarithmic concentration, and the correlation coefficients were 0.985, 0.979, and 0.950, respectively, which proved that the Au–Ag composite nanostructure with bottom Au layer can obtain an ultra-low detectable solubility of R6G molecules. The detection of ultra-low concentration analytes shows that the high-sensitivity *SERS* could be realized by the porous Au–Ag composite nanostructure. In addition, compared with the use of interference lithography [21] or 3D lithography [29], the preparation process used in this paper does not need to use sophisticated optical instruments.

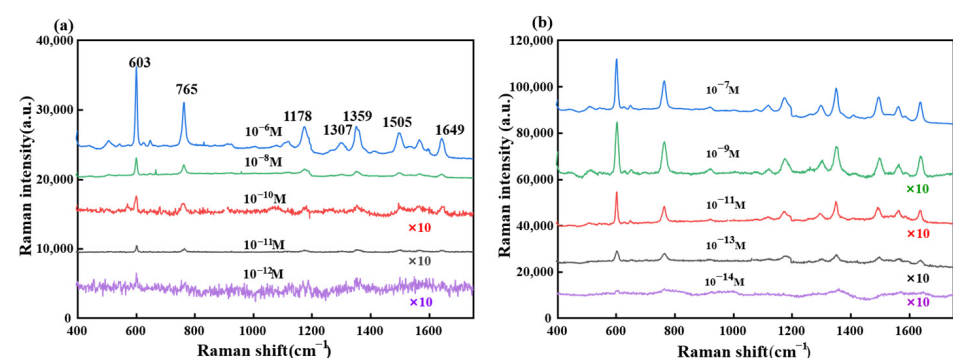


Figure 5. Raman spectra of (a) the composite Au–Ag nanostructures and (b) the composite Au–Ag nanostructures with the bottom Au mirror under different R6G molecule concentrations.

Here, the *SERS* and non-*SERS* spectra of the R6G molecules were measured, and the *EF* of the Au–Ag composite nanostructure were estimated by comparing the Raman intensity of the *SERS* signal and the non-*SERS* signal, as follows.

$$EF = \frac{I_{SERS}}{I_{non}} \times \frac{C_{non}}{C_{SERS}} \quad (1)$$

where C_{SERS} represents the concentration of R6G molecules immersed in aqueous solution and I_{SERS} represents the Raman intensities of the R6G molecule adhered to the Au–Ag composite nanostructure. Here, we measured the Raman spectrum of a silicon wafer treated by the R6G solution (0.5×10^{-5} M) and the *SERS* spectrum of the Au–Ag composite nanostructure sample treated by the R6G solution (10^{-12} M); at 765 cm^{-1} , I_{SERS} , I_{non} were 1462 and 534, respectively. Therefore, the *EF* of the 765 cm^{-1} Raman peak was calculated to be about 1.37×10^7 for the composite Au–Ag nanostructures. The *EF* of the Au–Ag composite nanostructure was much larger than that in many earlier reports with respect to porous Au–Ag hybrid nanoplates ($EF = 1.4 \times 10^6$) [22] and nano-sponges ($EF = 6.4 \times 10^5$) [42]. In addition, the *EF* of the Raman peak at 765 cm^{-1} for the Au–Ag nanostructures without underlying gold mirrors was estimated to be 2.4×10^5 . This indicated that high-sensitivity *SERS* substrates could be achieved by the facile fabrication of the Au–Ag composite nanostructures.

In addition, the uniformity is also an important parameter in special applications for the *SERS* substrate. 10^{-6} M R6G was taken as the molecule of detection. Figure 6a shows that the scanning area of a random position with an area of $50 \times 50 \mu\text{m}^2$ on the substrate was performed to estimate the uniformity, and 100 detection points was uniformly distributed on this square area. The Raman map of R6G at 765 cm^{-1} is shown in the Figure 6b, illustrating significant signal uniformity of the *SERS* substrate with the Au–Ag composite structure. Additionally, the average RSD of Raman intensity for the 765 cm^{-1} is 4.9%. The results indicate that a uniform *SERS* could be formed by the porous Au–Ag composite nanostructures.

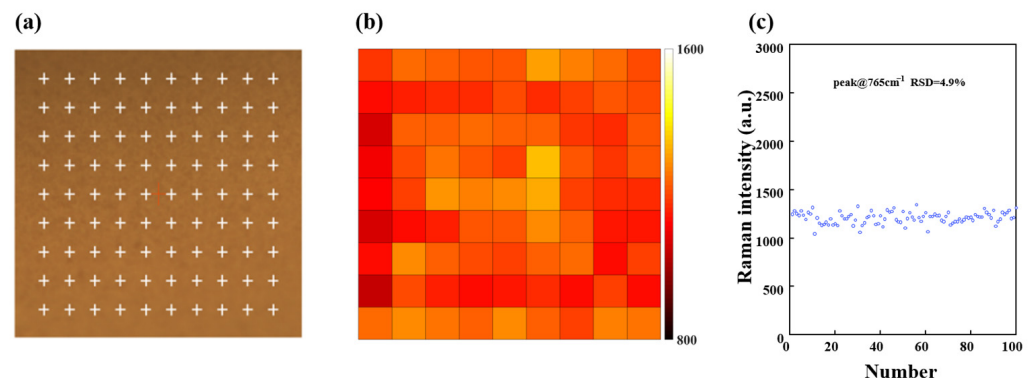


Figure 6. (a) The scanning area ($50 \times 50 \mu\text{m}^2$) of the Au–Ag composite structure covered by R6G molecule, the cross sign indicates the detection point. (b) *SERS* intensity mapping at 765 cm^{-1} . (c) The Raman intensity distribution at the 765 cm^{-1} peak.

4. Conclusions

In summary, this work developed a facile fabrication process route for a high-performance *SERS* substrate. After the deposition of the multilayer Au–Ag structure, annealing and dealloying techniques were performed to form a porous Au–Ag composite nanostructure. The results showed that the local electric field can be further enhanced by the *SERS* effect and the reflection of the underlying bottom Au. Furthermore, the corresponding results were also confirmed in the experiment. Compared with the use of modern precision optical instruments, the structure used in this paper can be prepared in a large area and the preparation process cost is lower. The *EF* of the R6G molecule detected by the *SERS*

substrate with the porous Au–Ag composite nanostructures reached 1.37×10^7 . It was expected to reach the level of single molecule detection. The *RSD* was as low as 4.9%. These advantages indicate that the Au–Ag composite structure scheme would provide a new opportunity for *SERS*-related detection with high uniformity and high sensitivity.

Author Contributions: Conceptualization, W.L. and Z.Y.; methodology, W.L. and Z.Y.; software, W.Z.; validation, X.H., W.L. and Z.Y.; formal analysis, K.W.; investigation, Y.Q.; resources, W.L. and X.H.; data curation, W.L. and Z.Y.; writing—original draft preparation, W.L. and Z.Y.; writing—review and editing, W.L., X.H. and Z.Y.; visualization, B.S.; supervision, W.L. and Z.Y.; project administration, W.L. and Z.Y.; funding acquisition, W.L. and Y.Q. All authors have read and agreed to the published version of the manuscript.

Funding: This work was supported by National Natural Science Foundation of China under Grants Numbers 61975037, 62275054, 62175039, 12004444 and 61904041.

Institutional Review Board Statement: Not applicable.

Informed Consent Statement: Not applicable.

Data Availability Statement: Not applicable.

Conflicts of Interest: The authors declare no conflict of interest.

References

- Baptista, P.; Pereira, E.; Eaton, P. Gold nanoparticles for the development of clinical diagnosis methods. *Anal. Bioanal. Chem.* **2008**, *391*, 943–950. [[CrossRef](#)] [[PubMed](#)]
- Lim, W.Q.; Gao, Z. Plasmonic nanoparticles in biomedicine. *Nano Today* **2016**, *11*, 168–188. [[CrossRef](#)]
- Zheng, T.; Li, G.G.; Li, F.Z.; Wu, R. Gold-Nanosponge-Based Multistimuli-Responsive Drug Vehicles for Targeted Chemo-Photothermal Therapy. *Adv. Mater.* **2016**, *28*, 8218–8226. [[CrossRef](#)] [[PubMed](#)]
- D’Acunto, M.; Cioni, P.; Gabellieri, E.; Presciutti, G. Exploiting gold nanoparticles for diagnosis and cancer treatments. *Nanotechnology* **2021**, *32*, 192001. [[CrossRef](#)] [[PubMed](#)]
- Yaseen, T.; Pu, H.; Sun, D.W. Functionalization techniques for improving SERS substrates and their applications in food safety evaluation: A review of recent research trends. *Trends Food Sci. Technol.* **2018**, *72*, 162–174.
- Feng, J.; Hu, Y.; Grant, E.; Lu, X. Determination of thiabendazole in orange juice using an MISPE-SERS chemosensor. *Food Chem.* **2018**, *239*, 816–822. [[CrossRef](#)]
- Wang, P.; Pang, S.; Pearson, B.; Chujo, Y. Rapid concentration detection and differentiation of bacteria in skimmed milk using surface enhanced Raman scattering mapping on 4-mercaptophenylboronic acid functionalized silver dendrites. *Anal. Bioanal. Chem.* **2017**, *409*, 2229–2238. [[CrossRef](#)]
- Hu, Y.; Feng, S.; Gao, F.; Li-Chan, E.C. Detection of melamine in milk using molecularly imprinted polymers-surface enhanced Raman spectroscopy. *Food Chem.* **2015**, *176*, 123–129. [[CrossRef](#)]
- Yang, Y.; Creedon, N.; O’Riordan, A.; Lovera, P. Surface Enhanced Raman Spectroscopy: Applications in Agriculture and Food Safety. *Photonics* **2021**, *8*, 568. [[CrossRef](#)]
- Yue, S.; Ye, W.; Xu, Z. SERS monitoring of the Fenton degradation reaction based on microfluidic droplets and alginate microparticles. *Analyst* **2019**, *144*, 5882–5889. [[CrossRef](#)]
- Yu, J.; Yang, M.; Li, Z.; Liu, C.; Wei, Y.; Zhang, C. Hierarchical particle-in-quasicavity architecture for ultratrace in situ Raman sensing and its application in real-time monitoring of toxic pollutants. *Anal. Chem.* **2020**, *92*, 14754–14761. [[CrossRef](#)] [[PubMed](#)]
- Pal, P.; Bonyár, A.; Veres, M.; Himics, L. A generalized exponential relationship between the surface-enhanced Raman scattering (SERS) efficiency of gold/silver nanoisland arrangements and their non-dimensional interparticle distance/particle diameter ratio. *Sens. Actuator A-Phys.* **2020**, *314*, 112225. [[CrossRef](#)]
- Xu, D.; Zhang, Y.; Zhang, S.; Yang, W.; Chen, J. Ultrasensitive SERS detection of crystal violet and malachite green based on high surface roughness copper nanocorns prepared via solid-state ionics method. *Sens. Actuator A-Phys.* **2021**, *331*, 113042. [[CrossRef](#)]
- Campion, A.; Kambhampati, P. Surface-enhanced Raman scattering. *Chem. Soc. Rev.* **1998**, *27*, 241–250.
- Liu, Z.; Yang, Z.; Peng, B.; Cao, C.; Zhang, H.Y. Highly sensitive, uniform, and reproducible surface-enhanced Raman spectroscopy from hollow Au–Ag alloy nanourchins. *Adv. Mater.* **2014**, *26*, 2431–2439. [[CrossRef](#)]
- Ebrahimzadeh Esfahani, N.; Kováč, J.; Kováčová, S.; Feile, M. Plasmonic Properties of the Metal Nanoparticles (NPs) on a Metal Mirror Separated by an Ultrathin Oxide Layer. *Photonics* **2023**, *10*, 78. [[CrossRef](#)]
- Barbillon, G. Au Nanoparticles Coated ZnO Film for Chemical Sensing by PIERS Coupled to SERS. *Photonics* **2022**, *9*, 562. [[CrossRef](#)]
- Lee, H.; Lee, J.H.; Jin, S.M.; Suh, Y.D.; Nam, J.M. Single-molecule and single-particle-based correlation studies between localized surface plasmons of dimeric nanostructures with ~1 nm gap and surface-enhanced Raman scattering. *Nano Lett.* **2013**, *13*, 6113–6121. [[CrossRef](#)]

19. Wang, D.; Zhu, W.; Chu, Y.; Crozier, K.B. High directivity optical antenna substrates for surface enhanced Raman scattering. *Adv. Mater.* **2012**, *24*, 4376–4380. [[CrossRef](#)] [[PubMed](#)]
20. Hatab, N.A.; Hsueh, C.H.; Gaddis, A.L.; Retterer, S.T. Free-standing optical gold bowtie nanoantenna with variable gap size for enhanced Raman spectroscopy. *Nano Lett.* **2010**, *10*, 4952–4955. [[CrossRef](#)]
21. Shen, Y.; Cheng, X.; Li, G.; Zhu, Q.; Chi, Z.; Wang, J. Highly sensitive and uniform surface-enhanced Raman spectroscopy from grating-integrated plasmonic nanoglass. *Nanoscale Horiz.* **2016**, *1*, 290–297. [[CrossRef](#)]
22. Wei, X.; Fan, Q.; Liu, H.; Bai, Y.; Zhang, L.; Zheng, H. Holey Au-Ag alloy nanoplates with built-in hotspots for surface-enhanced Raman scattering. *Nanoscale* **2016**, *8*, 15689–15695. [[CrossRef](#)]
23. Fu, Z.; Shen, Z.; Fan, Q.; Hao, S.; Wang, Y.; Liu, X. Preparation of multi-functional magnetic-plasmonic nanocomposite for adsorption and detection of thiram using SERS. *J. Hazard. Mater.* **2020**, *392*, 122356. [[CrossRef](#)]
24. Xu, J.; Du, J.; Jing, C.; Zhang, Y.; Cui, J. Facile detection of polycyclic aromatic hydrocarbons by a surface-enhanced Raman scattering sensor based on the Au coffee ring effect. *ACS Appl. Mater. Interfaces* **2014**, *6*, 6891–6897. [[CrossRef](#)] [[PubMed](#)]
25. Zhang, C.H.; Zhu, J.; Li, J.J.; Zhao, J.W. Small and sharp triangular silver nanoplates synthesized utilizing tiny triangular nuclei and their excellent SERS activity for selective detection of thiram residue in soil. *ACS Appl. Mater. Interfaces* **2017**, *9*, 17387–17398. [[CrossRef](#)]
26. Thacker, V.V.; Herrmann, L.O.; Sigle, D.O.; Zhang, T. DNA origami based assembly of gold nanoparticle dimers for surface-enhanced Raman scattering. *Nat. Commun.* **2014**, *5*, 3448. [[CrossRef](#)] [[PubMed](#)]
27. Niu, W.; Chua, Y.A.; Zhang, W.; Huang, H.; Lu, X. Highly Symmetric Gold Nanostars: Crystallographic Control and Surface-Enhanced Raman Scattering Property. *J. Am. Chem. Soc.* **2015**, *137*, 10460–10463. [[CrossRef](#)] [[PubMed](#)]
28. Lu, G.; Forbes, T.Z.; Haes, A.J. SERS detection of uranyl using functionalized gold nanostars promoted by nanoparticle shape and size. *Analyst* **2016**, *141*, 5137–5143. [[CrossRef](#)]
29. Fang, X.G.; Zheng, C.X.; Yin, Z.; Wang, Z.M. Hierarchically ordered silicon metastructures from improved self-assembly-based nanosphere lithography. *ACS Appl. Mater. Interfaces* **2020**, *12*, 12345–12352. [[CrossRef](#)]
30. Pisco, M.; Galeotti, F.; Grisci, G.; Quero, G. Self-assembled periodic patterns on the optical fiber tip by microsphere arrays. In Proceedings of the 24th International Conference on Optical Fibre Sensors, Curitiba, Brazil, 28 September–2 October 2015.
31. Tang, H.; Meng, G.; Li, Z.; Zhu, C.; Huang, Z.; Wang, Z. Hexagonally arranged arrays of urchin-like Ag hemispheres decorated with Ag nanoparticles for surface-enhanced Raman scattering substrates. *Nano Res.* **2015**, *8*, 2261–2270. [[CrossRef](#)]
32. Wu, G.; Cao, F.; Zhao, P.; Zhang, X.; Li, Z.; Yu, N. Novel periodic bilayer Au nanostructures for ultrasensitive surface-enhanced Raman spectroscopy. *Adv. Mater. Interfaces* **2018**, *5*, 1800820. [[CrossRef](#)]
33. Koya, A.N.; Zhu, X.; Ohannesian, N.; Yanik, A.A. Nanoporous metals: From plasmonic properties to applications in enhanced spectroscopy and photocatalysis. *ACS Nano* **2021**, *15*, 6038–6060. [[CrossRef](#)]
34. Liu, G.; Li, K.; Zhang, Y.; Du, J.; Ghafoor, S.; Lu, Y. A facile periodic porous Au nanoparticle array with high-density and built-in hotspots for SERS analysis. *Appl. Surf. Sci.* **2020**, *527*, 146807. [[CrossRef](#)]
35. Mandal, M.; Ranjan Jana, N.; Kundu, S.; Kumar Ghosh, S. Synthesis of Au-core–Ag-shell type bimetallic nanoparticles for single molecule detection in solution by SERS method. *J. Nanoparticle Res.* **2004**, *6*, 53–61. [[CrossRef](#)]
36. Gao, C.; Hu, Y.; Wang, M.; Chi, M.; Yin, Y. Fully alloyed Ag/Au nanospheres: Combining the plasmonic property of Ag with the stability of Au. *J. Am. Chem. Soc.* **2014**, *136*, 7474–7479. [[CrossRef](#)] [[PubMed](#)]
37. Zhang, T.; Sun, Y.; Hang, L.; Li, H.; Liu, G.; Zhang, X. Periodic Porous Alloyed Au-Ag Nanosphere Arrays and Their Highly Sensitive SERS Performance with Good Reproducibility and High Density of Hotspots. *ACS Appl. Mater. Interfaces* **2018**, *10*, 9792–9801. [[CrossRef](#)]
38. Liu, K.; Bai, Y.; Zhang, L.; Yang, Z.; Fan, Q.; Zheng, H. Porous Au–Ag Nanospheres with High-Density and Highly Accessible Hotspots for SERS Analysis. *Nano Lett.* **2016**, *16*, 3675–3681. [[CrossRef](#)]
39. Li, K.; Liu, G.; Zhang, S.; Dai, Y.; Ghafoor, S.; Huang, W. A porous Au-Ag hybrid nanoparticle array with broadband absorption and high-density hotspots for stable SERS analysis. *Nanoscale* **2019**, *11*, 9587–9592. [[CrossRef](#)]
40. Palik, E.D. *Handbook of Optical Constants of Solids II*; Academic Press: Boston, MA, USA, 1990; Volume 1, pp. 77–135.
41. Sharma, B.; Frontiera, R.R.; Henry, A.-I. SERS: Materials, applications, and the future. *Mater. Today* **2012**, *15*, 16–25. [[CrossRef](#)]
42. Yan, Y.; Radu, A.I.; Rao, W.; Wang, H. Mesoscopically Bi-continuous Ag–Au Hybrid Nanosponges with Tunable Plasmon Resonances as Bottom-Up Substrates for Surface Enhanced Raman Spectroscopy. *Chem. Mater.* **2016**, *28*, 7673–7682. [[CrossRef](#)]

Disclaimer/Publisher’s Note: The statements, opinions and data contained in all publications are solely those of the individual author(s) and contributor(s) and not of MDPI and/or the editor(s). MDPI and/or the editor(s) disclaim responsibility for any injury to people or property resulting from any ideas, methods, instructions or products referred to in the content.